THE JOURNAL OF BIOLOGICAL CHEMISTRY VOL. 287, NO. 44, pp. 36864–36872, October 26, 2012

Conformational Transitions Underlying Pore Opening and Desensitization in Membrane-embedded *Gloeobacter violaceus* Ligand-gated Ion Channel (GLIC)[S]

Received for publication, July 13, 2012, and in revised form, August 24, 2012 Published, JBC Papers in Press, September 13, 2012, DOI 10.1074/jbc.M112.401067

Phanindra Velisetty, Sreevatsa V. Chalamalasetti, and Sudha Chakrapani[1]

From the Department of Physiology and Biophysics, School of Medicine, Case Western Reserve University, Cleveland, Ohio 44106

Background: GLIC, a prokaryotic homologue of pentameric ligand-gated ion channels (LGIC), is activated by protons, and crystal structures suggest a putative open conformation.
Results: EPR-spectroscopic studies in the pore-lining segment reveals major conformational changes during activation and desensitization.
Conclusion: Gating mechanism in GLIC involves distinct activation and desensitization gates.
Significance: These studies provide insights into the role of structural dynamics in the functioning of LGIC.

Direct structural insight into the mechanisms underlying activation and desensitization remain unavailable for the pentameric ligand-gated channel family. Here, we report the structural rearrangements underlying gating transitions in membrane-embedded GLIC, a prokaryotic homologue, using site-directed spin labeling and electron paramagnetic resonance (EPR) spectroscopy. We particularly probed the conformation of pore-lining second transmembrane segment (M2) under conditions that favor the closed and the ligand-bound desensitized states. The spin label mobility, intersubunit spin-spin proximity, and the solvent-accessibility parameters in the two states clearly delineate the underlying protein motions within M2. Our results show that during activation the extracellular hydrophobic region undergoes major changes involving an outward translational movement, away from the pore axis, leading to an increase in the pore diameter, whereas the lower end of M2 remains relatively immobile. Most notably, during desensitization, the intervening polar residues in the middle of M2 move closer to form a solvent-occluded barrier and thereby reveal the location of a distinct desensitization gate. In comparison with the crystal structure of GLIC, the structural dynamics of the channel in a membrane environment suggest a more loosely packed conformation with water-accessible intrasubunit vestibules penetrating from the extracellular end all the way to the middle of M2 in the closed state. These regions have been implicated to play a major role in alcohol and drug modulation. Overall, these findings represent a key step toward understanding the fundamentals of gating mechanisms in this class of channels.

Fast synaptic transmission at the central and peripheral nervous systems are mediated by pentameric ligand-gated ion channels (LGICs).[2] Upon binding neurotransmitter, these channels rapidly switch from closed to open conformation, and prolonged neurotransmitter exposure drives the channel to a nonconducting desensitized state. Understanding the structural details of molecular motions underlying gating transitions has been a main focus in the field. Recent discovery of bacterial homologues of the LGIC family (1) have paved way to determination of high resolution crystal structures and have provided a valuable structural framework for elucidating eukaryotic LGIC function (2–4). When expressed in heterologous systems, the *Gloeobacter violaceus* homologue (GLIC) was found to be activated by protons (5), and the *Erwinia chrysanthemi* homologue (ELIC) was activated by primary amines (6). The crystal structures of ELIC in the absence of ligand (3) and GLIC at acidic pH (2, 4) revealed distinct conformational differences, and thereby were proposed to represent the closed and open states, respectively. Although high resolution structures of ELIC in the open and GLIC in the closed conformation have not been resolved, current models of channel gating are based on direct comparison of these two end states. Despite limited sequence identity, there is considerable conservation of key residues in the pore lining M2 segment among GLIC, ELIC, and nAChR channels. Specifically, M2 is organized into the following: an intracellular ring of Glu(−2′) that forms the selectivity filter region (7, 8), two rings of polar residues (Thr(2′)-Ser(6′)), and three rings of hydrophobic residues (Ile(9′)-Val(17′) at the extracellular end. Aligning GLIC and ELIC structures shows that the extracellular hydrophobic end of M2 has a much wider pore diameter in GLIC in comparison with the ELIC structure, suggesting that channel opening involves tilt translational motion (2–4). However, curiously enough, a comparison of this region in GLIC with the electron micrograph derived structure of the Torpedo ray nAChR, in membranes without ligand, reveals no major differences. This raises the question of whether channel closure involves small changes reflecting the nAChR structure or large changes as predicted by the ELIC structure. Although recently solved crystal structures of cysteine cross-linked GLIC, stabilized in a locally closed conformation, suggest that movements leading to channel closing might more closely follow the ELIC structure (9). Furthermore, there is also considerable discrep-

[S] This article contains supplemental Figs. 1–3.

[1] To whom correspondence should be addressed: 10900 Euclid Ave., Robbins Bldg., E620, Cleveland, OH 44106. Tel.: 216-368-3875; Fax: 216-238-3952; E-mail: sudha.chakrapani@case.edu.

[2] The abbreviations used are: LGIC, ligand-gated ion channel; GLIC, *Gloeobacter violaceus* ligand-gated ion channel; NiEDDA, Ni(II) ethylenediaminediacetic acid; nAChR, nicotinic acetylcholine receptor.

ancy at the functional level surrounding GLIC gating properties. GLIC activation in oocytes and HEK cells reveal slow opening kinetics and currents that do not decay over an extended period of time. However, two groups report that GLIC desensitizes, albeit with very different kinetics (10, 11). In a recent report, we showed by patch clamp measurements that purified and reconstituted GLIC rapidly activates and deactivates (~ms) in response to pH changes and desensitized relatively slowly (~s) during sustained pH pulses. Furthermore, GLIC desensitization is not only modulated by factors in a manner analogous to its eukaryotic counterpart but also shows structural conservation of the changes in a key region in the extracellular domain of channel during agonist-bound desensitization (12). The structural and functional similarity, along with comparable drug sensitivity, makes GLIC an attractive system to serve as a structural archetype for the eukaryotic LGIC (13–18). Here, we have investigated the structural rearrangement in the pore-lining M2 segment during activation and desensitization of GLIC reconstituted into lipid bilayers by site-directed spin labeling and EPR spectroscopy. Changes in spin-label dynamics, proximity, and accessibility to lipid and water phases were studied under basic and acidic pH conditions that stabilize channels in the closed and ligand-bound desensitized conformations, respectively. Our findings reveal that the pore region of GLIC in the closed state more closely resembles the ELIC structure and the recently crystallized locally closed conformation of GLIC, whereas at the same time, they suggest differences in the tightness of helical packing on the membrane. Under acidic pH, our data point toward the presence of two distinct activation and desensitization gates in the channel, thereby illustrating the M2 movements associated with major gating events in GLIC.

EXPERIMENTAL PROCEDURES

Protein Expression and Purification—The GLIC gene cloned into a modified pET26b vector was expressed as a fusion construct with N-terminal maltose binding protein as described previously (2, 4). Briefly, BL21(DE3) *Escherichia coli* cells transformed with the construct were grown in Terrific Broth medium containing 50 μg/ml kanamycin at 37 °C to A_{600} of 1.0. Cells were induced with 0.2 mM isopropyl 1-thio-β-D-galactopyranoside overnight at 20 °C. Membranes were prepared by homogenizing the cells in 150 mM NaCl, 20 mM Tris base, pH 7.4 (buffer A), with protease inhibitors and centrifuged at 100,000 × *g* for 1 h. Membranes were solubilized in buffer A using 40 mM *n*-dodecyl-β-D-maltopyranoside (Anatrace) at 4 °C. GLIC was purified by binding to amylose resin and eluting with 20 mM maltose. The maltose binding protein tag was cleaved with human rhino virus 3C protease (GE Healthcare), and the GLIC protein was separated using size exclusion chromatography on a Superdex 200 10/300 column (GE Healthcare).

Membrane Reconstitution and Electrophysiology—Electrophysiological measurements were made by patch clamp recordings in channel-reconstituted liposomes prepared as described previously (12, 19–21). Purified protein was reconstituted into preformed asolectin vesicles by diluting in 150 mM NaCl, 10 mM HEPES, pH 7.0 (reconstitution buffer). Detergent was removed by incubating the proteoliposome suspension with Biobeads (Bio-Rad). The suspension was centrifuged at 100,000 × *g* for 1 h, and the pellet was resuspended in reconstitution buffer. A drop of the proteoliposome was placed on a glass slide and dried overnight in a desiccator at 4 °C. The sample was then rehydrated with 20 μl of buffer, which yielded giant liposomes. GLIC was reconstituted in 1:10,000 protein: lipid (molar ratio) for macroscopic currents. Currents were measured using inside out patch clamp of proteoliposomes in symmetrical NaCl. All experiments were performed at room temperature. Recording pipettes were pulled from thin walled borosilicate glass and heat polished to a resistance of 1.5–2 megohms and filled with 150 mM NaCl, 10 mM HEPES, pH 8.0. Low pH was obtained using 10 mM sodium citrate buffer. Currents were elicited in response to pH jumps using an RCS-200 fast solution exchanger (switch time, 2 ms) fed by gravity (Biologic). Currents were measured using Axopatch 200B, digitized at 10 kHz sampling frequency, and were analyzed using Clampfit (version 10.2).

Site-directed Spin Labeling and EPR Spectroscopy—The native Cys (Cys-26) was mutated to Ser, and single Cys mutants in M2 were generated using the Cys-free construct (C26S) as the template. Purified protein was labeled with a methanethiosulfonate spin probe 1-oxyl-2,2,5,5-tetramethylpyrrolidin-3-yl) methyl methanethiosulfonate (Toronto Research) at a 10:1 label:protein molar ratio. The efficiency of labeling was calculated by first measuring the absolute protein concentration in detergent and then determining the concentration of the spin label in the sample using a standard curve of known concentrations of 2,2,6,6-tetramethyl-1-piperidinyloxy *versus* peak area (from double integration of the EPR signal) (22, 23). Spin-labeled samples were reconstituted at a 1:3000 protein:lipid (molar ratio) in a mixture of asolectin, incubated with Biobeads, and centrifuged to obtain a pellet of the proteoliposomes. pH changes were made by equilibrating the liposomes at 42 °C with appropriate buffers in a water bath. The sample was centrifuged, and the process was repeated multiple times to ensure complete buffer exchange. Continuous wave-EPR measurements were performed at room temperature on a Bruker EMX X-band spectrometer equipped with a dielectric resonator and a gas permeable TPX plastic capillary. First, derivative absorption spectra were recorded at an incident microwave power of 2.0 milliwatts, modulation frequency of 100 kHz, and modulation amplitude of 1.0 gauss. Our analyses were centered on three types of dynamic EPR structural information (24–29). First, the mobility of the spin probe, calculated as the inverse of the central line width of the first derivative absorption spectra (ΔH_o^{-1}). This parameter is governed both by the local steric contacts in the immediate vicinity of the probe and by the flexibility of the backbone to which it is attached (30). As the frequency of nitroxide rotational motion is reduced, as witnessed during the formation of tertiary or quaternary contacts, the line width and hence ΔH_o^{-1} increases for any particular motional geometry. On the contrary, structural motions leading to an increase in the freedom of movement of the probe are reflected as a decrease in ΔH_o^{-1}. Second, the proximity between intersubunit spins, estimated from amplitudes of the EPR signal. The spectral line shapes and the amplitudes of the signal are affected

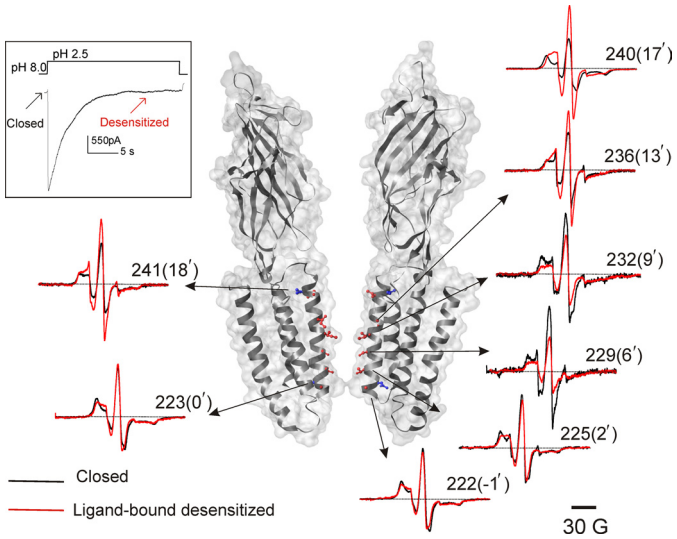

FIGURE 1. **Structural rearrangement underlying channel activation and desensitization.** GLIC activates in response to extracellular low pH pulses and undergoes desensitization under prolonged exposure (*inset*). Representative continuous wave-EPR spectra of positions in M2 are shown displaying changes in amplitude and line shapes in response to pH changes. *Black* and *red traces* were obtained from channels in the closed (pH 8.0) and in the desensitized conformation (pH 2.5), respectively. In each case, the spectra are normalized to the total number of spin. Spin-labeled positions are highlighted by CPK presentation, with residues facing the pore shown in *red* and those facing away from the pore shown in *blue*. Only two subunits are shown for clarity.

by the extent of through space short range spin-spin dipolar coupling between spin labels within the multimeric protein. Third, spin probe solvent accessibility was evaluated by collisional relaxation methods. Here, non-polar molecular oxygen (ΠO_2) serves as a contrast agent to evaluate solvent exposure (membrane and water), whereas polar Ni(II) ethylenediaminediacetic acid (ΠNiEDDA) reports the extent of aqueous exposure (25, 31, 32). The accessibility to NiEDDA (100 mM) for the desensitized state was measured at pH 3.0 instead of 2.5 due to the instability of the complex at very acidic pH. The accessibility parameter (Π) is estimated from power saturation experiments in which the vertical peak-to-peak amplitude of the central line of the first derivative EPR spectra is measured as a function of increasing incident microwave power (25).

RESULTS

Conformational Transitions Monitored by EPR Spectroscopy—To study the conformational changes in the pore-lining M2 segment by EPR spectroscopy, individual Cys mutations in M2 were made in the cysteine-free background (C26S). Each mutant was purified, spin-labeled, and subjected to gel-filtration chromatography. Only those mutants that displayed a stable monodisperse peak corresponding to the pentameric channel (22 of 25 mutants tested) were used for further analysis (supplemental Fig. 1*A*). Using FRET-based assays and electrophysiological measurements (12), we previously showed that asolectin membranes maintain GLIC in a monodisperse population and support pH-mediated conformational changes from closed to open to desensitized conformations (Fig. 1, *inset*). We therefore carried out all our EPR measurements of spin-labeled GLIC reconstituted into asolectin vesicles. We verified the functionality of several cysteine mutants in the presence of spin label by measuring pH-elicited macroscopic currents (supplemental Fig. 1*B*). All of the mutants studied showed rapid activation in response to jumps to acidic pH and a time-dependent decay of current due to desensitization with some differences in the kinetics of desensitization in comparison to WT. This finding is not unexpected given that mutations in M2 have been reported to alter gating properties (33–36). Because EPR measurements were carried out under steady-state conditions of pH 8.0 and 2.5, despite differences in fast kinetics, GLIC mutants are expected to reside predominantly in their closed and ligand-bound desensitized conformations, respectively. Fig. 1 shows representative spectra (normalized to reflect equal number of spin) from residues in M2 in the closed (*black*, pH 8.0) and ligand-bound desensitized (*red*, pH 2.5) conformations. In the closed state, all of the measured positions show line shapes characteristic of motionally restricted spin labels, which is indicative of an overall sterically packed environment of M2 in this conformation. Furthermore, the EPR line shapes at a number of pore-facing residues (notably, at sites 222(−1′), 223(0′), 228(5′), 229(6′), 236(13′), 239(16′), and 240(17′)) reveal broadening by short range dipolar coupling arising from intersubunit proximity (supplemental Fig. 2). It is important to note that, as a likely consequence of poor labeling efficiency due to steric hindrance in narrow cavities, the extent of spectral broadening due to dipolar interaction might be underestimated. The efficiency of labeling for sites 219(−4′), 224(1′), 225(2′), and 240(17′) were determined to be 60, 55, 40, and 90%, respectively (see "Experimental Procedures"), suggesting that steric constraints might limit the number of labels per pentamer to ≤2 in the middle of M2. A simple visual inspection suggests that pore-facing residues at either end of the helix show similar extent of immobilization (position 220(−3′) *versus* 240(17′), side chains shown in *red* CPK), whereas for residues facing away from the pore, the intracellular end of M2 appears to be more constrained in comparison (position 223(0′) *versus* 241(18′), side chains shown in *blue* CPK). Upon switching to pH 2.5, residues beyond the 232(9′) position showed a dramatic decrease in broadening and concomitant increase in amplitude, demonstrating that residues in this region move farther from each other. However, residues in the intracellular end (residues 219(−4′)-224(1′)) show minimal change, whereas residues in between the ends show a decrease in the amplitude of the signal, suggesting that these regions move closer or undergo no movement, respectively.

To quantify through-space intersubunit spin-spin dipolar coupling, we calculated Ω parameter (37) as the ratio of spin-normalized amplitudes of the central resonance line in the desensitized and closed conformations. The Ω values lower than 1 indicate that the spin-labeled residues move closer to the symmetry axis, whereas values > 1 reflect motions away from the axis. The Ω profile (presented in log scale to highlight the polarity of changes) for M2 residues during channel gating is shown in Fig. 2*A*, and these values are color coded and mapped on GLIC structure in Fig. 2*B*. Residues between 219(-4′) and 224(1′), comprising the selectivity filter region, show no major change in Ω values, suggesting that this region (gray block in Fig. 2, *A* and *B*) does not undergo significant movement. Inter-

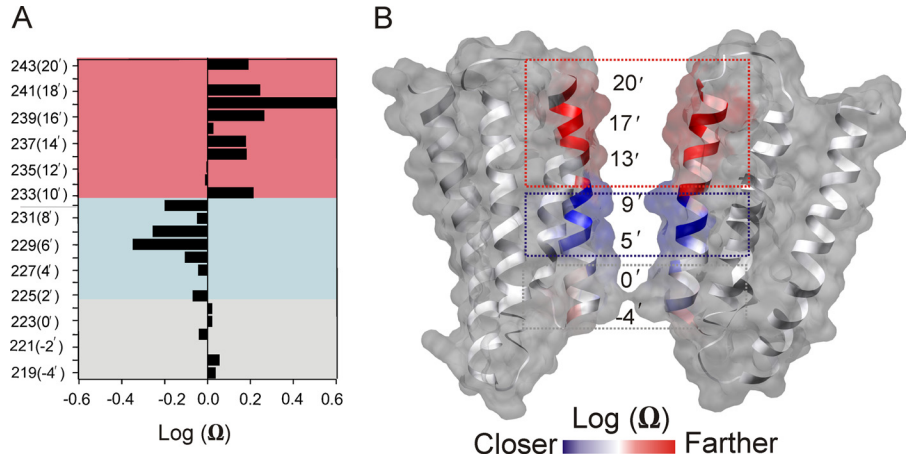

FIGURE 2. **Changes in the spin label proximity during gating.** *A*, profile of changes in the amplitude of the EPR signal reflecting differences in the spin-spin dipolar coupling in the closed and desensitized conformation. For positions with log $\Omega < 0$, the proximity between individual spin labels increases as the side chains get closer toward the pore axis and for log $\Omega > 0$, the spin labels move away from the pore axis and further apart from each other. In each case, the same sample is used for both closed and desensitized state measurements. *B*, the log Ω parameter mapped on to the GLIC crystal structure. Residues displayed in *red* and *blue* show positive and negative log Ω values, respectively. Residues colored in *white* show values closer to 0. The *boxed* areas highlight regions moving away, getting closer and regions of no significant movement.

estingly, the region immediately above (residues 227(4′)-232(9′)), consisting mostly of polar residues) shows a decrease in Ω, presumably resulting from these residues moving closer toward the pore axis (*blue blocks*). Additionally, the largest change in Ω occurs at the extracellular end of M2 in the hydrophobic region (comprising of residues 233(10′)-243(20′)), suggesting that this region tilts away radially during channel opening. Overall, these results indicate that channel activation involves movement of the hydrophobic region, which thereby forms the activation gate, and the polar region immediately below undergoes a tighter packing during desensitization and contributes to the desensitization gate of the channel.

pH Dependence of the Conformational Changes at the Activation Gate—We then studied the pH dependence of M2 movement and compared it with the pH dependence of channel activation as measured from the peak values of macroscopic currents responses (12). We chose residue 240(17′), in the extracellular hydrophobic region, to follow the M2 movement and measured changes in the EPR signal as a function of sequentially decreasing the pH. Fig. 3*A* shows spin-normalized spectra (to represent the same number of spins) and amplitude-normalized spectra (to the peak amplitude) for each pH condition. The spectral properties, both in terms of amplitude (Fig. 3*A*, *left*) and broadening (Fig. 3*A*, *right*) showed a gradual change in the range pH 6 to 3, with minimal changes for pH values lower than 3. A plot of pH dependence of the EPR signal amplitude and of the ionic current measurements (Fig. 3*B*) shows that both parameters follow a similar trend except that the former precedes the functional measurements by ~1 pH unit. This is not surprising considering that ion conduction involving full channel opening might require protonation of multiple subunits, whereas EPR measurements track the conformational changes in individual subunits even prior to complete channel activation. It is also likely that differences in proton affinity in the active (measured by electrophysiology) and desensitized conformation (measured by EPR) contributed to such an effect. EPR studies and Rb^+ flux assays in KcsA also report a similar feature, suggesting that these findings denote

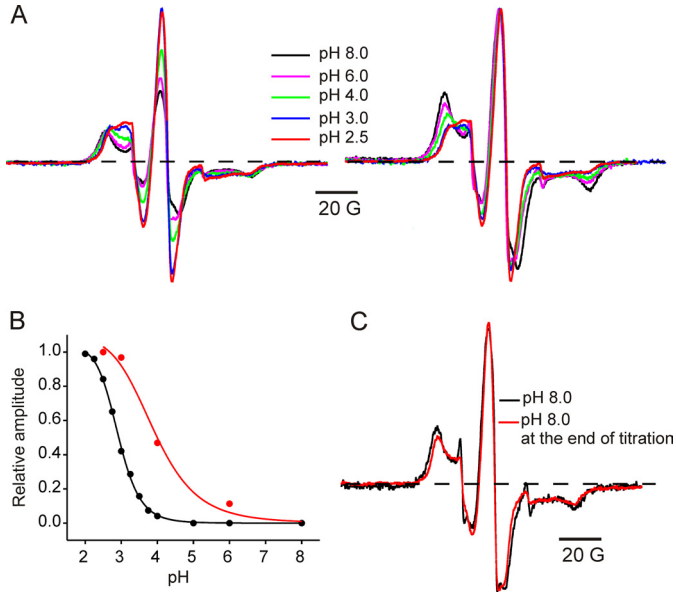

FIGURE 3. **pH-dependent conformational changes at the activation gate monitored by position 240 movements.** *A*, EPR line shapes obtained after sequentially equilibrating the sample with the indicated pH starting with pH 8.0. In each case, the spectra are normalized to the number of spin. *B*, pH dependence of EPR signal amplitude (*red*) overlaid with the pH dependence of the maximal peak response from macroscopic current measurements (*black*). The pK_a of maximal response are 3.9 + 0.2 and 2.9 + 0.1 for the EPR and current measurements, respectively. *C*, samples were returned to pH 8.0 at the end of sequential pH change. Overlapping spectra shows reversibility of the spectral line shapes.

analogous mechanisms for multimeric channels (37). Samples subjected to sequential pH changes toward more acidic conditions were then equilibrated back to pH 8.0, and the EPR spectra were compared with spectra at the beginning of the experiment (Fig. 3*C*). In accordance with functional measurements (12), the conformational changes reported by the EPR signals are also fully reversible.

Changes in Solvent Accessibility Parameters—To correlate structural properties of GLIC in a lipid bilayer with its detergent-stabilized crystal structure, the EPR enviromental param-

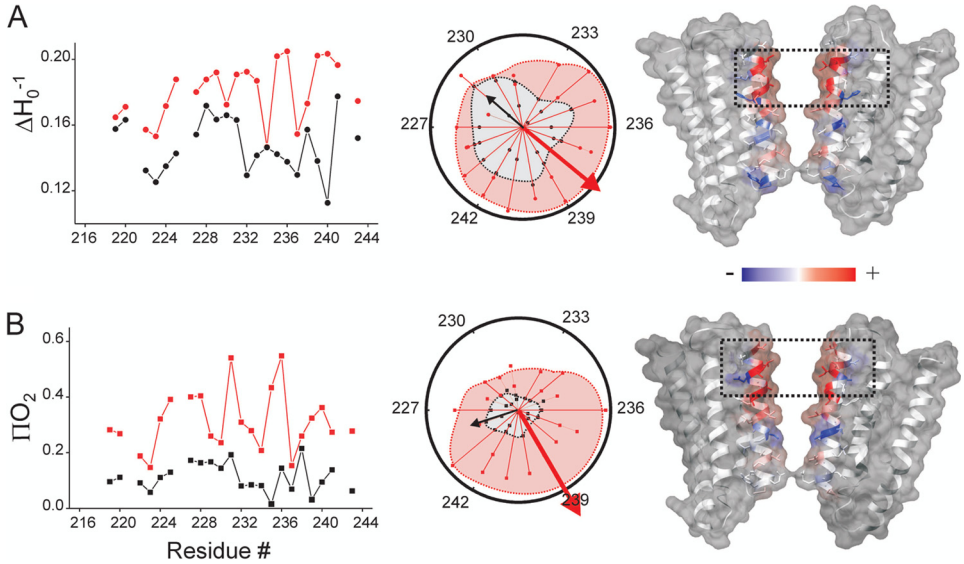

FIGURE 4. **Changes in the residue enviromental parameters.** *A*, mobility ΔH_o^{-1}. *B*, O_2 accessibility ΠO_2 for the closed (*black*) and desensitized (*red*) states. Shown is the profile of changes in the enviromental parameters for the M2 residues (*left*). Shown is a helical wheel representation of the mobility and accessibility superimposed in a polar coordinate (*middle*). The resultant vector of the individual ΔH_o^{-1} or ΠO_2 values points toward the more mobile or solvent accessible face of the helix. The shaded area within the *dashed lines* highlights the projection for complete set of accessibility data relative to the maximal accessibility vector. Fractional differences (normalized to the maximum value measured within each data set) in the ΔH_o^{-1} and ΠO_2 values for the closed and desensitized states mapped on the GLIC structure and color coded, with *red* denoting an increase and *blue* representing a decrease in the environmental parameter (*right*).

eters were mapped and color-coded on the GLIC crystal structures. Fig. 4, *A* and *B*, show the probe mobility ($\Delta H_o^{-1)}$ (*top*) and O_2 accessibility values (ΠO_2) (*bottom*) for the entire M2 segment in the closed (*black*) and ligand-bound desensitized (*red*) conformation (see "Experimental Procedures"). Both mobility and O_2 accessibility in the intracellular part of M2 reports a complex and rather restrictive environment with a gradual increase in local dynamics and accessibility toward the extracellular half. The pore-lining residues do not show any O_2 accessibility, suggesting that in the closed state this side of the helix faces a solvent-occluded environment. Upon activation, a much more pronounced periodicity in the spectral properties is evident as is expected of the M2 segment now exposed to a more asymmetric environment in the open channel: solvent exposed pore-lining face and a relatively solvent-excluded face pointing toward the rest of the transmembrane helices. This feature is highlighted by superimposing mobility and accessibility values on a helical wheel polar representation, and the direction of the calculated ΔH_o^{-1} and ΠO_2 moments points toward the face of the helix that is more dynamic and solvent exposed, respectively (Fig. 4, *middle*). It is interesting to note that the direction of the resultant vector points toward the face of the helix that is away from the pore lumen in the closed conformation and switches toward the lumen in the ligand-bound conformation. The location and extent of these conformational rearrangements can be visualized by mapping the differences between the closed and desensitized states (each normalized to the corresponding maximum value within the data set) onto the GLIC structure. As seen with changes in the amplitude, the extracellular end shows an increase in motional freedom and accessibility (residues color-coded in *red*), the polar intermediate region shows a decrease in the corresponding values (in *blue*), and the intracellular selectivity region shows minimal changes (in *white*). Overall, the transition to the open (and eventually desensitized) conformation in GLIC is accompanied by large structural changes at the extracellular half of M2 with minimal changes at the intracellular end. This suggests that extracellular end of M2 moves away from the 5-fold symmetry axis and increases the diameter of the permeation pathway, whereas the intermediate region moves closer during desensitization.

Aqueous Vestibules within Transmembrane Helices—An inspection of accessibility to polar agent (ΠNiEDDA) in the closed state shows that the pore-lining residues in M2 are fully buried and isolated from water, whereas residues pointing away from the pore lumen are water accessible (Fig. 5*A*, *top panels*). In this conformation, the orientation of the resultant vector indeed points toward M2 residues facing away from the pore (residue 231(8′)). Upon activation, the pore facing residues now show a periodic increase in NiEDDA accessibility from the extracellular end up to the 232(9′) position (Fig. 5*B*, *bottom panels*, supplemental Fig. 3*A*). A comparison of the NiEDDA accessibility in this conformation to the calculated solvent accessibility values for the GLIC structure shows remarkable agreement in the periodic trend (supplemental Fig. 3*B*). Furthermore, the face of M2 pointing away from the pore lumen loses its accessibility to NiEDDA except for residue 238(15′) (supplemental Fig. 3), which shows significant water accessibility in both conformations. A decrease in water accessibility behind the channel-lining face of M2 is somewhat expected if the M2 segment were to move away radially during activation, thereby reducing the intrasubunit cavity volume. It is necessary to mention that due to the larger size of NiEDDA, in comparison with water molecules (~13 times larger than water), the aqueous accessibility measured by collisional quenching could be an underestimation of the actual depths of water penetra-

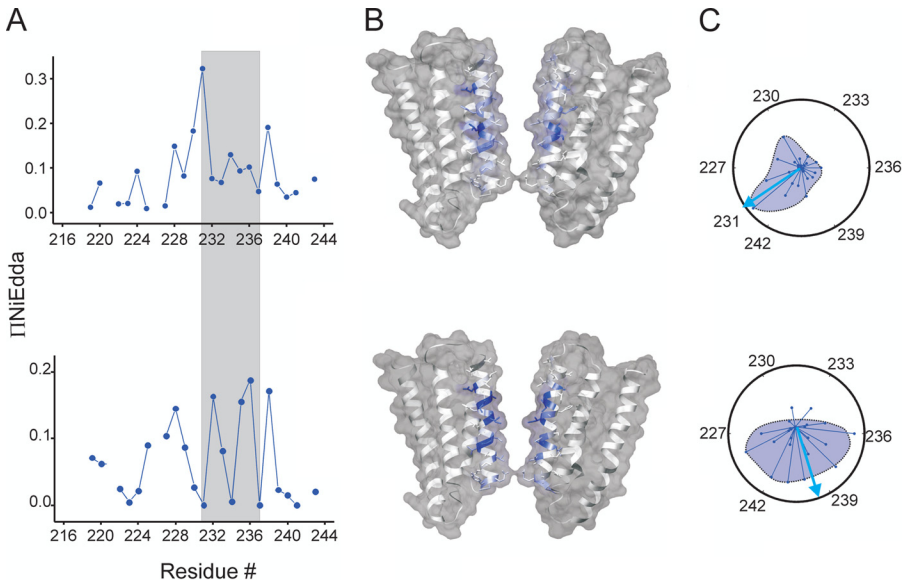

FIGURE 5. **Aqueous vestibules in the closed and in the desensitized states.** *A*, ΠNiEDDA values for the M2 residues in the closed (*top*) and desensitized states (*bottom*). The *gray boxed* area highlights regions of maximal change between the two states. *B*, ΠNiEDDA values mapped on the GLIC structure reveals differences in the solvent accessible vestibules in the two conformations. *C*, changes in the ΠNiEDDA moment during gating conformational change.

tion. Nevertheless, these findings strongly argue for a water-filled cavity within the helical bundle behind M2 that likely tapers off shortly after residue 225(2′) in the closed state and also suggest a more loose packing of helices relative to each other in the extracellular end of the channel.

DISCUSSION

A complete understanding of ion channel structure-function relationships mandates high resolution structural information of the channel in different functional states. Although the pore structures of ligand-bound GLIC (2, 4) and GluCL (38) are similar to each other and closely comparable with the unliganded nAChR conformation, they are distinctly different from the unliganded ELIC structure (3). There are two major questions that arise: first, what conformational rearrangements underlie GLIC activation and does the closed state of GLIC more closely resemble ELIC or nAChR structure? A closer resemblance to ELIC would imply that GLIC undergoes much larger protein motions during activation, whereas similarity to nAChR would mean GLIC experiences more subtle changes. Second, to what functional state of GLIC gating does the crystal structure correspond? It is well known that in eukaryotic LGIC channels, the conformational changes leading to transitions between the closed, open, and desensitized states are critically governed by membrane lipid composition (39–42). We previously showed that GLIC function is also modulated by membrane lipids in an analogous way (12). Based on these functional measurements and using conditions that favor channel activation and desensitization, we measured protein movements in the M2 regions that underlie these gating events. The EPR data of GLIC in acidic pH show general similarities with the overall arrangement of M2 as seen in the crystal structures, especially in the wide open extracellular and tightly packed intracellular end (2, 4). Minimal changes in the EPR signal in the region between −2′ to 2′ compared with the closed and open/desensitized states suggest that there are minimal structural rearrangements, and GLIC maintains a narrow pore in this region during gating. A model of narrow intracellular constriction is also consistent with findings from substituted cysteine accessibility studies (43) and from measurements of single channel block by protonation of ionizable residues in the pore (43, 44). The more striking findings from our studies are the differences evident in the polar midregion that appears to be more constrained than in the crystal structure. Based on low steady-state currents in macroscopic recordings under similar conditions (12), we suggest that these differences likely indicate a more pronounced desensitized state on the membrane. Comparing the two conformations monitored by EPR with the currently available structures of GLIC trapped in its putatively open (2, 4) and locally closed state (9) reveal insights into the activation mechanism. In the closed conformation, pore-facing residues at the extracellular end in GLIC experience a motionally restricted, solvent-excluded environment, similar to the residues at the intracellular end. Therefore, channel closure in GLIC (Fig. 6) involves movement of the external M2 regions closer together, in a way depicted by the ELIC structure and in agreement with the recently crystallized locally closed GLIC structure (9). The locally closed structure of GLIC, achieved by cysteine bridges in the extracellular end of M2, shares most of the features of the potentially open structure except a locally closed pore (9). Increased solvent accessibility observed beyond the 9′ is also consistent with a bend at this position both in this conformation of GLIC and the ELIC structure. In the closed conformation, the M2 segment is tightly packed between −2′ to 2′ position with the rest of the protein, thereby limiting access to solvent. In contrast to ELIC, the helical packing in GLIC in the closed conformation creates a deep water-accessible vestibule behind M2 that extends roughly to the middle of the membrane (closer to the 2′ position). Substituted cysteine accessibility measurements in GLIC also show accessibilities that reflect a loosely packed M2 on the membrane (11), and the locally closed

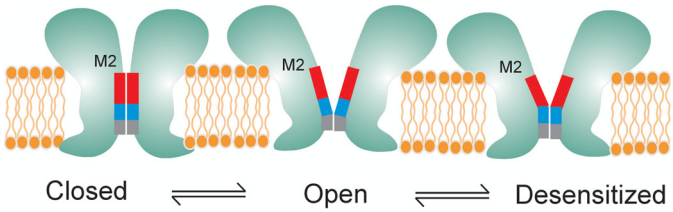

FIGURE 6. **Schematic representation of speculative gating motions in M2 during transitions between closed, open, and desensitized conformations.** The blocks represent the hydrophobic (*red*), the polar (*blue*), and the charged selectivity filter region (*gray*).

structure of GLIC also reveals a much wider vestibule within the transmembrane segments (9). Furthermore, the NiEDDA accessibility of 15′ residue (facing away from the pore lumen) in both the closed and desensitized conformations is interesting and is consistent with water exposure of the equivalent position in nAChR, $GABA_A$, and glycine receptors (44–46). The water-filled vestibule lined by the 15′ residue has been implicated in anesthetic and alcohol modulation in this class of channels (15–17, 45, 46).

Despite decades of extensive investigation, mechanisms underlying desensitization remains poorly understood. Desensitization in LGIC (47) is thought to play diverse roles, from governing neural networks associated with memory and learning process (48, 49) to regulating non-neuronal cell functions such as cell growth control and modulation of immune response (50). Abnormalities in desensitization underlie several disease conditions such as autosomal dominant nocturnal frontal lobe epilepsy and congenital myasthenic syndrome and have also been implicated in nicotine addiction and lung cancer (51–56). In particular, positive allosteric modulators of nAChR, which potentiate channel function by slowing desensitization, are being developed as a possible therapeutic strategy in the treatment of Alzheimer disease, schizophrenia, depression, and pain (50, 57). However, the mechanisms by which agonists and allosteric ligands modulate structural changes that lead to channel opening and desensitization remain unclear. Our findings suggest that the desensitization gate involves residues between 2′-9′ coming closer to occlude permeation such that in the desensitized conformation the narrow part of the channel extends from the selectivity filter further until the 9′ region (Fig. 6). In remarkable agreement, cysteine reactivity to modifying agents in this region of nAChR was found to decrease during desensitization (43), suggesting that barrier to conduction extends below the 9′ position. We previously showed that binding of lidocaine not only blocks GLIC currents in a voltage-dependent manner but also slows desensitization (12). Crystal structure of GLIC in the presence of lidocaine analogue reveals a binding site in M2 such that the polar group and the hydrophobic tail might interact with the 6′ and 9′ positions, respectively. Consistent with our earlier suggestion, the effect of lidocaine on GLIC desensitization might be through a "foot-in-the-door" type of mechanism (58), where binding of lidocaine prevents the 6′–9′ region from coming closer. Furthermore, the 9′ position is highly conserved across the LGIC family and mutations at the 9′ residue in several LGIC members, including GLIC, affecting desensitization and lidocaine binding (34, 59–61). It is also interesting to note that the GLIC structure in the putative open state reveals a bundle of six detergent molecules (dodecylmaltoside *n*-dodecyl-β-D-maltopyranoside) within the pore such that one molecule per subunit interacts with the hydrophobic rings of GLIC, and the other molecule is oriented in the opposite direction close to the 6′–9′ positions (4). Binding of hydrophobic blockers in the pore region alters channel gating properties, and therefore, it is indeed likely that these bulky molecules might play a role in stabilizing putative open conformation of the channel. Overall, the presence of distinct activation and desensitization gates are in line with earlier predictions in nAChR (62, 63).

Although our techniques provide unique advantage to investigate structural changes in a membrane environment that also allows for simultaneous functional measurements, there are indeed several caveats that need to be taken into consideration, particularly those arising as a consequence of cysteine mutations and introduction of spin label. Further complexities also arise from differences in the extent of labeling in the narrow parts of the channel. Nevertheless, these findings set the stage for a thorough understanding of protein motions underlying gating and modulation in GLIC.

In summary, we show details of GLIC activation and desensitization mechanism in a membrane bound environment that facilitates these conformational transitions. Structural changes associated with gating in GLIC mirror many conserved features within the LGIC family and therefore offer a convenient tool to pair up detailed structure-functional studies in this class of channels.

Acknowledgments—We are very grateful to Dr. Witold Surewicz for critical reading and comments on the manuscript. We thank Dr. Raimund Dutzler for the GLIC clone.

REFERENCES

1. Tasneem, A., Iyer, L. M., Jakobsson, E., and Aravind, L. (2005) Identification of the prokaryotic ligand-gated ion channels and their implications for the mechanisms and origins of animal Cys-loop ion channels. *Genome Biol.* **6,** R4
2. Hilf, R. J., and Dutzler, R. (2009) Structure of a potentially open state of a proton-activated pentameric ligand-gated ion channel. *Nature* **457,** 115–118
3. Hilf, R. J., and Dutzler, R. (2008) X-ray structure of a prokaryotic pentameric ligand-gated ion channel. *Nature* **452,** 375–379
4. Bocquet, N., Nury, H., Baaden, M., Le Poupon, C., Changeux, J. P., Delarue, M., and Corringer, P. J. (2009) X-ray structure of a pentameric ligand-gated ion channel in an apparently open conformation. *Nature* **457,** 111–114
5. Bocquet, N., Prado de Carvalho, L., Cartaud, J., Neyton, J., Le Poupon, C., Taly, A., Grutter, T., Changeux, J. P., and Corringer, P. J. (2007) A prokaryotic proton-gated ion channel from the nicotinic acetylcholine receptor family. *Nature* **445,** 116–119
6. Zimmermann, I., and Dutzler, R. (2011) Ligand activation of the prokaryotic pentameric ligand-gated ion channel ELIC. *PLoS Biol.* **9,** e1001101
7. Imoto, K., Busch, C., Sakmann, B., Mishina, M., Konno, T., Nakai, J., Bujo, H., Mori, Y., Fukuda, K., and Numa, S. (1988) Rings of negatively charged amino acids determine the acetylcholine receptor channel conductance. *Nature* **335,** 645–648
8. Corringer, P. J., Bertrand, S., Galzi, J. L., Devillers-Thiéry, A., Changeux, J. P., and Bertrand, D. (1999) Mutational analysis of the charge selectivity filter of the α7 nicotinic acetylcholine receptor. *Neuron* **22,** 831–843
9. Prevost, M. S., Sauguet, L., Nury, H., Van Renterghem, C., Huon, C.,

Poitevin, F., Baaden, M., Delarue, M., and Corringer, P. J. (2012) A locally closed conformation of a bacterial pentameric proton-gated ion channel. *Nat. Struct. Mol. Biol.* **19,** 642–649
10. Gonzalez-Gutierrez, G., and Grosman, C. (2010) Bridging the gap between structural models of nicotinic receptor superfamily ion channels and their corresponding functional states. *J. Mol. Biol.* **403,** 693–705
11. Parikh, R. B., Bali, M., and Akabas, M. H. (2011) Structure of the M2 transmembrane segment of GLIC, a prokaryotic Cys loop receptor homologue from *Gloeobacter violaceus*, probed by substituted cysteine accessibility. *J. Biol. Chem.* **286,** 14098–14109
12. Velisetty, P., and Chakrapani, S. (2012) Desensitization mechanism in prokaryotic ligand-gated ion channel. *J. Biol. Chem.* **287,** 18467–18477
13. Goyal, R., Salahudeen, A. A., and Jansen, M. (2011) Engineering a prokaryotic Cys-loop receptor with a third functional domain. *J. Biol. Chem.* **286,** 34635–34642
14. Duret, G., Van Renterghem, C., Weng, Y., Prevost, M., Moraga-Cid, G., Huon, C., Sonner, J. M., and Corringer, P. J. (2011) Functional prokaryotic-eukaryotic chimera from the pentameric ligand-gated ion channel family. *Proc. Natl. Acad. Sci. U.S.A.* **108,** 12143–12148
15. Weng, Y., Yang, L., Corringer, P. J., and Sonner, J. M. (2010) Anesthetic sensitivity of the *Gloeobacter violaceus* proton-gated ion channel. *Anesth. Analg.* **110,** 59–63
16. Howard, R. J., Murail, S., Ondricek, K. E., Corringer, P. J., Lindahl, E., Trudell, J. R., and Harris, R. A. (2011) Structural basis for alcohol modulation of a pentameric ligand-gated ion channel. *Proc. Natl. Acad. Sci. U.S.A.* **108,** 12149–12154
17. Nury, H., Van Renterghem, C., Weng, Y., Tran, A., Baaden, M., Dufresne, V., Changeux, J. P., Sonner, J. M., Delarue, M., and Corringer, P. J. (2011) X-ray structures of general anaesthetics bound to a pentameric ligand-gated ion channel. *Nature* **469,** 428–431
18. Hilf, R. J., Bertozzi, C., Zimmermann, I., Reiter, A., Trauner, D., and Dutzler, R. (2010) Structural basis of open channel block in a prokaryotic pentameric ligand-gated ion channel. *Nat. Struct. Mol. Biol.* **17,** 1330–1336
19. Delcour, A. H., Martinac, B., Adler, J., and Kung, C. (1989) Modified reconstitution method used in patch clamp studies of *Escherichia coli* ion channels. *Biophys. J.* **56,** 631–636
20. Cortes, D. M., Cuello, L. G., and Perozo, E. (2001) Molecular architecture of full-length KcsA: role of cytoplasmic domains in ion permeation and activation gating. *J. Gen. Physiol.* **117,** 165–180
21. Chakrapani, S., Cordero-Morales, J. F., and Perozo, E. (2007) A quantitative description of KcsA gating I: macroscopic currents. *J. Gen. Physiol.* **130,** 465–478
22. Gross, A., Columbus, L., Hideg, K., Altenbach, C., and Hubbell, W. L. (1999) Structure of the KcsA potassium channel from *Streptomyces lividans*: a site-directed spin labeling study of the second transmembrane segment. *Biochemistry* **38,** 10324–10335
23. Koteiche, H. A., Reeves, M. D., and McHaourab, H. S. (2003) Structure of the substrate binding pocket of the multidrug transporter EmrE: site-directed spin labeling of transmembrane segment 1. *Biochemistry* **42,** 6099–6105
24. Altenbach, C., Marti, T., Khorana, H. G., and Hubbell, W. L. (1990) Transmembrane protein structure: spin labeling of bacteriorhodopsin mutants. *Science* **248,** 1088–1092
25. Farahbakhsh, Z. T., Altenbach, C., and Hubbell, W. L. (1992) Spin labeled cysteines as sensors for protein-lipid interaction and conformation in rhodopsin. *Photochem. Photobiol.* **56,** 1019–1033
26. Altenbach, C., Greenhalgh, D. A., Khorana, H. G., and Hubbell, W. L. (1994) A collision gradient method to determine the immersion depth of nitroxides in lipid bilayers: application to spin-labeled mutants of bacteriorhodopsin. *Proc. Natl. Acad. Sci. U.S.A.* **91,** 1667–1671
27. Hubbell, W. L., Mchaourab, H. S., Altenbach, C., and Lietzow, M. A. (1996) Watching proteins move using site-directed spin labeling. *Structure* **4,** 779–783
28. Hubbell, W. L., Cafiso, D. S., and Altenbach, C. (2000) Identifying conformational changes with site-directed spin labeling. *Nat. Struct. Biol.* **7,** 735–739
29. Altenbach, C., Froncisz, W., Hemker, R., McHaourab, H., and Hubbell, W. L. (2005) Accessibility of nitroxide side chains: absolute Heisenberg exchange rates from power saturation EPR. *Biophys. J.* **89,** 2103–2112
30. Mchaourab, H. S., Lietzow, M. A., Hideg, K., and Hubbell, W. L. (1996) Motion of spin-labeled side chains in T4 lysozyme. Correlation with protein structure and dynamics. *Biochemistry* **35,** 7692–7704
31. Gross, A., and Hubbell, W. L. (2002) Identification of protein side chains near the membrane-aqueous interface: a site-directed spin labeling study of KcsA. *Biochemistry* **41,** 1123–1128
32. Perozo, E., Cortes, D. M., and Cuello, L. G. (1998) Three-dimensional architecture and gating mechanism of a K^+ channel studied by EPR spectroscopy. *Nat. Struct. Biol.* **5,** 459–469
33. Cymes, G. D., Grosman, C., and Auerbach, A. (2002) Structure of the transition state of gating in the acetylcholine receptor channel pore: a phi-value analysis. *Biochemistry* **41,** 5548–5555
34. Revah, F., Bertrand, D., Galzi, J. L., Devillers-Thiéry, A., Mulle, C., Hussy, N., Bertrand, S., Ballivet, M., and Changeux, J. P. (1991) Mutations in the channel domain alter desensitization of a neuronal nicotinic receptor. *Nature* **353,** 846–849
35. Wang, H. L., Cheng, X., and Sine, S. M. (2012) Intramembrane proton binding site linked to activation of bacterial pentameric ion channel. *J. Biol. Chem.* **287,** 6482–6489
36. Labarca, C., Nowak, M. W., Zhang, H., Tang, L., Deshpande, P., and Lester, H. A. (1995) Channel gating governed symmetrically by conserved leucine residues in the M2 domain of nicotinic receptors. *Nature* **376,** 514–516
37. Perozo, E., Cortes, D. M., and Cuello, L. G. (1999) Structural rearrangements underlying K^+-channel activation gating. *Science* **285,** 73–78
38. Hibbs, R. E., and Gouaux, E. (2011) Principles of activation and permeation in an anion-selective Cys-loop receptor. *Nature* **474,** 54–60
39. daCosta, C. J., and Baenziger, J. E. (2009) A lipid-dependent uncoupled conformation of the acetylcholine receptor. *J. Biol. Chem.* **284,** 17819–17825
40. Colón-Sáez, J. O., and Yakel, J. L. (2011) The α7 nicotinic acetylcholine receptor function in hippocampal neurons is regulated by the lipid composition of the plasma membrane. *J. Physiol.* **589,** 3163–3174
41. Barrantes, F. J. (2002) Lipid matters: nicotinic acetylcholine receptor-lipid interactions (Review). *Mol. Membr. Biol.* **19,** 277–284
42. Sunshine, C., and McNamee, M. G. (1992) Lipid modulation of nicotinic acetylcholine receptor function: the role of neutral and negatively charged lipids. *Biochim. Biophys. Acta* **1108,** 240–246
43. Wilson, G., and Karlin, A. (2001) Acetylcholine receptor channel structure in the resting, open, and desensitized states probed with the substituted-cysteine-accessibility method. *Proc. Natl. Acad. Sci. U.S.A.* **98,** 1241–1248
44. Cymes, G. D., Ni, Y., and Grosman, C. (2005) Probing ion-channel pores one proton at a time. *Nature* **438,** 975–980
45. Williams, D. B., and Akabas, M. H. (1999) γ-Aminobutyric acid increases the water accessibility of M3 membrane-spanning segment residues in γ-aminobutyric acid type A receptors. *Biophys. J.* **77,** 2563–2574
46. Mascia, M. P., Trudell, J. R., and Harris, R. A. (2000) Specific binding sites for alcohols and anesthetics on ligand-gated ion channels. *Proc. Natl. Acad. Sci. U.S.A.* **97,** 9305–9310
47. Katz, B., and Thesleff, S. (1957) A study of the desensitization produced by acetylcholine at the motor end-plate. *J. Physiol.* **138,** 63–80
48. Giniatullin, R., Nistri, A., and Yakel, J. L. (2005) Desensitization of nicotinic ACh receptors: shaping cholinergic signaling. *Trends Neurosci.* **28,** 371–378
49. Jones, M. V., and Westbrook, G. L. (1995) Desensitized states prolong GABAA channel responses to brief agonist pulses. *Neuron* **15,** 181–191
50. Donnelly-Roberts, D., Bertrand, D., and Gopalakrishnan, M. (2011) Nicotinic acetylcholine receptors as therapeutic targets: emerging frontiers in basic research and clinical science–editorial comments. *Biochem. Pharmacol.* **82,** 797
51. Ochoa, E. L., Chattopadhyay, A., and McNamee, M. G. (1989) Desensitization of the nicotinic acetylcholine receptor: molecular mechanisms and effect of modulators. *Cell Mol. Neurobiol.* **9,** 141–178
52. Scuka, M., and Mozrzymas, J. W. (1992) Postsynaptic potentiation and desensitization at the vertebrate end-plate receptors. *Prog. Neurobiol.* **38,** 19–33
53. Weiland, S., Witzemann, V., Villarroel, A., Propping, P., and Steinlein, O.

(1996) An amino acid exchange in the second transmembrane segment of a neuronal nicotinic receptor causes partial epilepsy by altering its desensitization kinetics. *FEBS Lett.* **398,** 91–96
54. Kuryatov, A., Gerzanich, V., Nelson, M., Olale, F., and Lindstrom, J. (1997) Mutation causing autosomal dominant nocturnal frontal lobe epilepsy alters Ca^{2+} permeability, conductance, and gating of human $\alpha4\beta2$ nicotinic acetylcholine receptors. *J. Neurosci.* **17,** 9035–9047
55. Milone, M., Wang, H. L., Ohno, K., Fukudome, T., Pruitt, J. N., Bren, N., Sine, S. M., and Engel, A. G. (1997) Slow-channel myasthenic syndrome caused by enhanced activation, desensitization, and agonist binding affinity attributable to mutation in the M2 domain of the acetylcholine receptor α subunit. *J. Neurosci.* **17,** 5651–5665
56. Bertrand, S., Weiland, S., Berkovic, S. F., Steinlein, O. K., and Bertrand, D. (1998) Properties of neuronal nicotinic acetylcholine receptor mutants from humans suffering from autosomal dominant nocturnal frontal lobe epilepsy. *Br. J. Pharmacol.* **125,** 751–760
57. Gopalakrishnan, M., Bertrand, D., and Williams, M. (2007) Nicotinic acetylcholine receptors as therapeutic targets: emerging frontiers in basic research and clinical science - editorial comments. *Biochem. Pharmacol.* **74,** 1091
58. Armstrong, C. M. (1971) Interaction of tetraethylammonium ion derivatives with the potassium channels of giant axons. *J. Gen. Physiol.* **58,** 413–437
59. Chang, Y., and Weiss, D. S. (1998) Substitutions of the highly conserved M2 leucine create spontaneously opening rho1 γ-aminobutyric acid receptors. *Mol. Pharmacol.* **53,** 511–523
60. Yakel, J. L., Lagrutta, A., Adelman, J. P., and North, R. A. (1993) Single amino acid substitution affects desensitization of the 5-hydroxytryptamine type 3 receptor expressed in *Xenopus oocytes*. *Proc. Natl. Acad. Sci. U.S.A.* **90,** 5030–5033
61. Gonzalez-Gutierrez, G., Lukk, T., Agarwal, V., Papke, D., Nair, S. K., and Grosman, C. (2012) Mutations that stabilize the open state of the *Erwinia chrisanthemi* ligand-gated ion channel fail to change the conformation of the pore domain in crystals. *Proc. Natl. Acad. Sci. U.S.A.* **109,** 6331–6336
62. Auerbach, A., and Akk, G. (1998) Desensitization of mouse nicotinic acetylcholine receptor channels. A two-gate mechanism. *J. Gen. Physiol.* **112,** 181–197
63. Purohit, Y., and Grosman, C. (2006) Block of muscle nicotinic receptors by choline suggests that the activation and desensitization gates act as distinct molecular entities. *J. Gen. Physiol.* **127,** 703–717